A highly ionized stellar bow shock in the Small Magellanic Cloud

WILLIAM J. HENNEY,[1] S. JANE ARTHUR,[1] AND M. VALERDI[2]

[1]*Instituto de Radioastronomía y Astrofísica, Universidad Nacional Autónoma de México, Apartado Postal 3-72, 58090 Morelia, Michoacán, Mexico*
[2]*Instituto Nacional de Astrofísica, Óptica y Electrónica, Luis Enrique Erro #1, Tonantzintla, 72840 Puebla, México*

Abstract

We report the discovery of a parsec-scale stellar bow shock associated with the O2 III(f) star Walborn 3 in the cluster NGC 346 of the Small Magellanic Cloud. The bow shock is most clearly detected in optical He II and [Ar IV] emission lines but is also seen at mid-infrared wavelengths between $12\,\mu$m and $24\,\mu$m. There is no evidence that the star is a runaway, rather the bow shock is likely due to interaction of the stellar wind with streaming motions of the photoionized gas within the N66 H II region.

Keywords: Atomic physics; Circumstellar matter; Stars: winds, outflows

1. INTRODUCTION

The interaction of a star's wind with the surrounding medium can result in an arc-shaped circumstellar emission nebula, frequently referred to as a bow shock (Gull & Sofia 1979; van Buren & McCray 1988). Stellar bow shocks are found around a wide variety of different stars, including pre-main sequence stars (Bally & Reipurth 2001; Henney et al. 2013), neutron stars (Cordes et al. 1993), and cool giants and supergiants (Sahai & Chronopoulos 2010; Cox et al. 2012), but they are most commonly associated with hot luminous OB stars (van Buren et al. 1995; Kobulnicky et al. 2016). Bow shocks are most frequently observed via their infrared continuum emission (Meyer et al. 2016), which arises from dust grains that are heated by the stellar radiation field (Draine & Li 2007), but specific classes of bow shock have also been identified via multiple thermal and non-thermal emission mechanisms that trace gas and plasma components. The emission arcs are most commonly interpreted as due to the hydrodynamic interaction induced by supersonic relative motion of the star with respect to the ambient material (Wilkin 1996), but models involving a subsonic interaction have also been proposed (Mackey et al. 2015, 2016). Also, the role of the stellar wind ram pressure in supporting the arc may be replaced by radiation pressure in some cases, see Henney & Arthur (2019a,b,c).

Stellar bow shocks can be used to estimate stellar wind mass loss rates by applying momentum-balance arguments

w.henney@irya.unam.mx

Corresponding author: William J. Henney

(Gvaramadze et al. 2012; Kobulnicky et al. 2018, 2019; Henney & Arthur 2019c). These provide an important check on more traditional spectroscopic methods (Hillier 2020), since the systematic uncertainties and biases are different. Line-driven wind theory for hot stars predicts that momentum-loss rates should increase with metallicity, Z, as $\dot{M}V_{\rm w} \propto Z^n$ with $n = 0.6$–0.8 (Vink et al. 2001; Krtička & Kubát 2018; Vink & Sander 2021; Björklund et al. 2021) for the most luminous stars ($L > 10^6\,{\rm L}_\odot$).

The closest low-metallicity stellar populations ($Z = 0.1$ to $0.2Z_\odot$, Narloch et al. 2021) are found in the Small Magellanic Cloud (SMC) at a distance of $62\,$kpc (Graczyk et al. 2020). A small number of stellar bow shocks have been previously identified in the SMC (Gvaramadze et al. 2011; Sheets et al. 2013) by means of their mid-infrared dust emission. The majority of these sources are found far from the cores of dense clusters and are probably *runaways* (Blaauw 1961), which have been ejected from a binary system or stellar cluster (Hoogerwerf et al. 2001; Renzo et al. 2019). In the Milky Way, a second class of stellar bow shocks are found inside young massive star clusters: *weather vanes* (Povich et al. 2008), which have low space velocities and are interacting with streaming motions of the local interstellar medium, such as champagne flows (Tenorio-Tagle 1979).

In this paper, we report the discovery of just such a bow shock inside the massive stellar cluster NGC 346, which excites the H II region N66 (Henize 1956). The bow shock is associated with the very early-type star Walborn 3 (W 3) (Walborn & Blades 1986), also known as MPG 355 (Massey et al. 1989) with spectral type ON2 III(f*) (Heydari-Malayeri & Selier 2010).
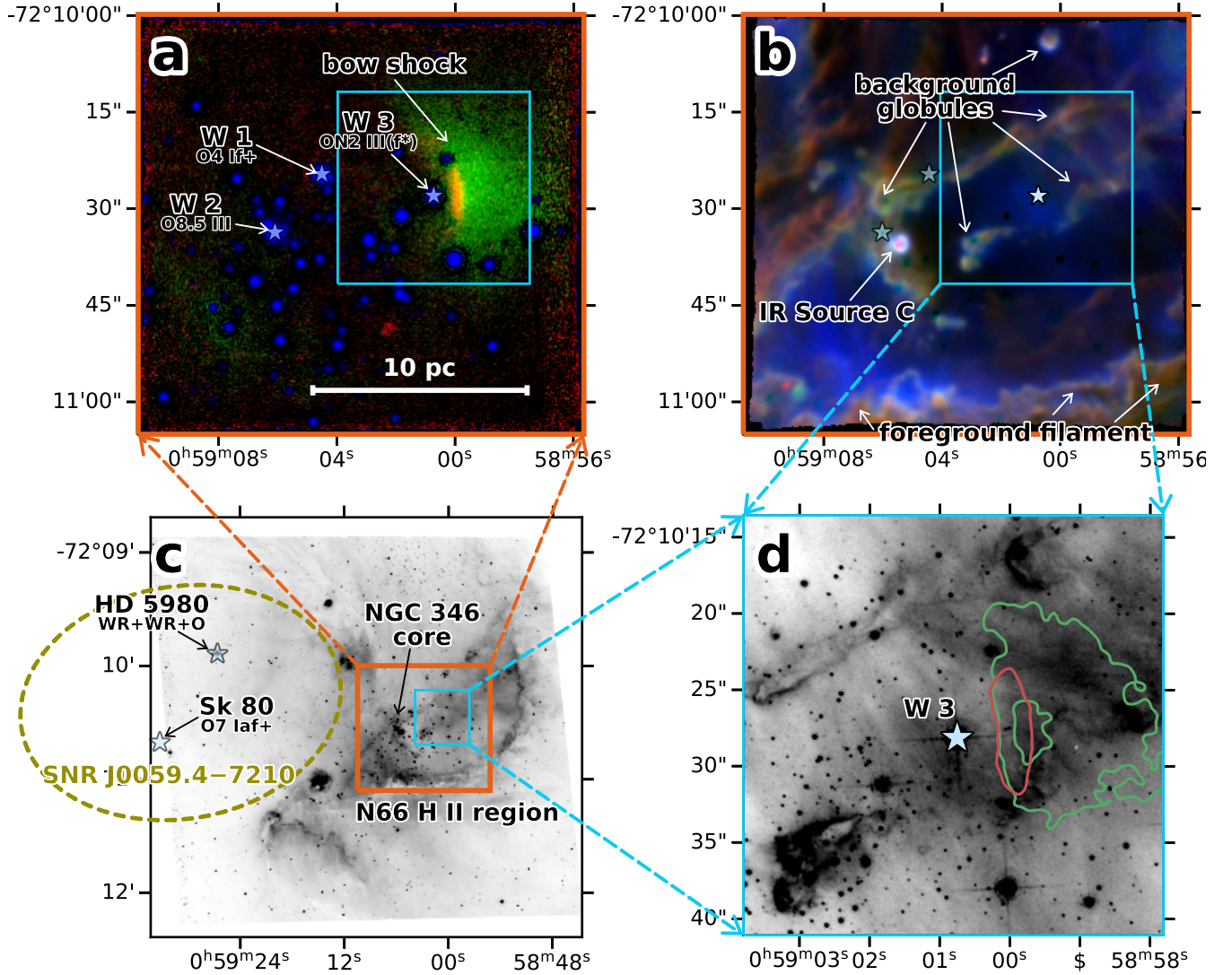
Atmosphere models of Rivero González et al. (2012)

Figure 1. MUSE emission line images of the core of NGC 346. (a) High-ionization emission from the bow shock. Red shows He II $\lambda4686$, green shows [Ar IV] $\lambda4740$, blue shows continuum emission at 4700 Å (mainly starlight). Star symbols indicate the positions of the most luminous ionizing stars in the cluster: Walborn 1, 2, and 3. (b) Medium to low-ionization emission from the surrounding N66 H II region. Red shows [O I] $\lambda6300$, green shows [S II] $\lambda6731$, blue shows [S III] $\lambda9069$. (c) Location of the MUSE field within the wider nebula against a background Hα image from HST-ACS in the F658N filter. The yellow dashed ellipse shows the maximum extent of the X-ray emission from the supernova remnant SNR J59.4−7210, while star symbols indicate more distant luminous ionizing stars. (d) Zoom of panel c showing detail of the bow shock region in the light of Hα emission, with superimposed contours of He II (red) and [Ar IV] (green).
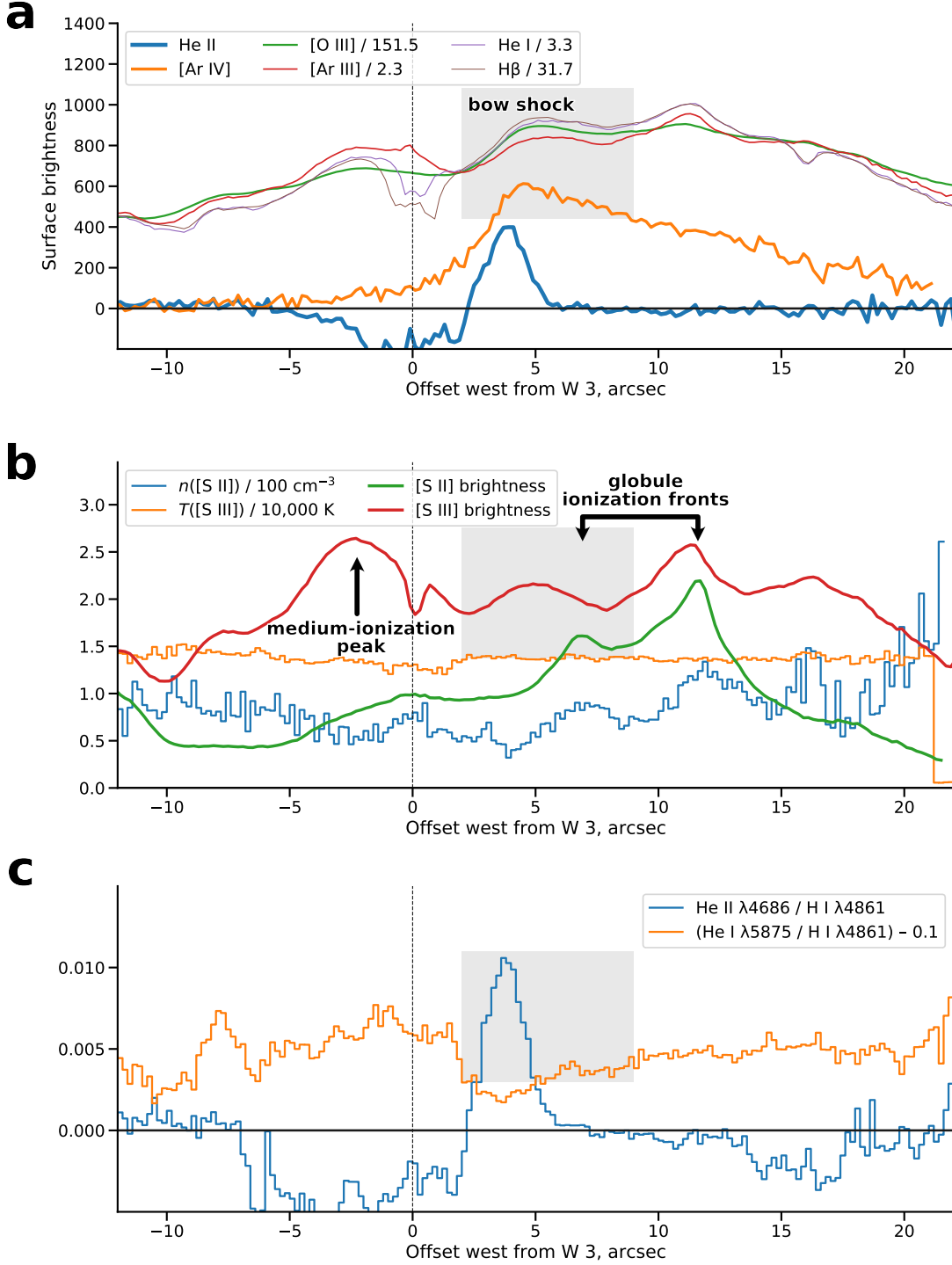
Figure 2. (a) Continuum-subtracted and extinction-corrected line surface brightness profiles along an East–West cut along the bow shock axis of width 4 arcsec, derived from MUSE integral field spectra. The gray box indicates the leading edge of the bow shock emission for comparison with following figures. Thickest lines show the high ionization emission from He II λ4686 (blue) and [Ar IV] λ4740 (orange). Progressively thinner lines show medium ionization emission from [O III] λ5007 (green), [Ar III] λ7136 (red), He I λ5875 (purple), and Hβ λ4861 (brown). Vertical scale gives brightness in instrument units, for conversion to cgs multiply by 1.489×10^{-8} erg s^{-1} cm^{-2} sr^{-1}. The brightness of medium ionization lines have been scaled by factors given in the key, so as to make all the lines approximately coincide at the left edge of the gray box. (b) As panel a but showing the [S II] density (orange) and [S III] temperature (blue), together with the brightness profiles of [S II] λ6731 (red) and [S II] λ9069 (green) on an arbitrary scale. (c) As panel a but showing line ratios of He II/H I (blue) and He I/H I (orange). A constant value of 0.1 has been subtracted from the latter for ease of comparison and to emphasise the slight dip in He I/H I at the position of the bow shock.
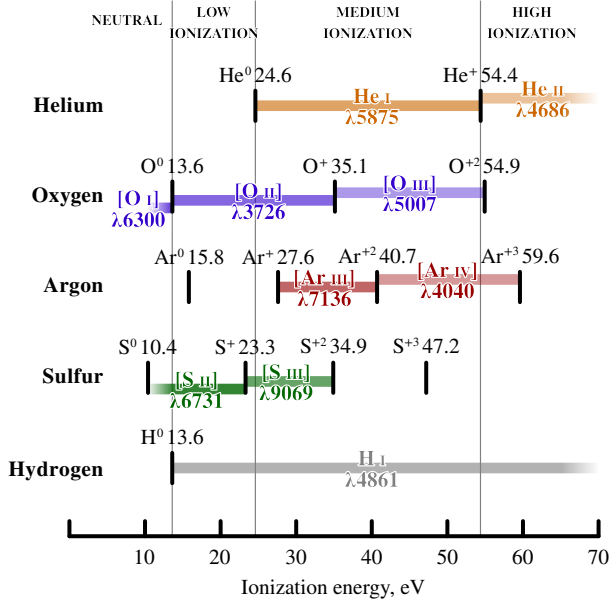
Figure 3. Classification of optical emission lines by degree of ionization. The broad ionization zones are defined by the H and He opacity: neutral ($H^0 + He^0$), low ionization ($H^+ + He^0$), medium ionization ($H^+ + He^+$), and high ionization ($H^+ + He^{+2}$). Within each zone, the ionization of metals will vary according to the local ionizing flux spectrum and electron density, depending on the ionization energy of each ion. The latter is indicated in the figure for selected elements, together with the range of ionization where different lines will be emitted, assuming that forbidden lines are excited solely by electron collisions, while permitted lines are excited solely by recombinations.

2. OBSERVATIONS

The primary observational data set used in this paper is an archival integral field spectral cube of NGC 346 obtained with the MUSE spectrograph (Bacon et al. 2010, 2014) on the VLT as part of program 098.D-0211(A) (PI: W.-R. Hamann). The usable field of view is approximately 64 arcsec times 60 arcsec with spaxel size of 0.2 arcsec and estimated seeing full-width half maximum (FWHM) width of 0.961 arcsec. The spectral range is 4595 Å to 9366 Å sampled at 1.25 Å pix^{-1} and the spectral resolving power varies from $R \approx 2000$ in the blue to $R \approx 4000$ in the red. We use reduced data from the standard ESO pipeline processing (Weilbacher et al. 2020), co-added across multiple observations obtained on 2016-08-22 with a total effective exposure time of 12 600 s.

We divide the spectral range into sections of width 800 Å and fit a 6th order polynomial to the continuum in line-free wavelengths of each section, using an independent fit for each spaxel. We then extract individual emission lines (or close blends) from the continuum-subtracted spectra using 5 Å windows, centered on the expected wavelength of each line in the systemic frame of the nebula (heliocentric velocity $V \approx 160 \, \mathrm{km \, s^{-1}}$). We correct for an over-subtraction of the sky background, which is apparent in the pipeline-processed data cube. We establish accurate zero points for all lines by checking that multiple line ratios tend towards physically reasonable asymptotes as the brightness tends towards zero.

We use the observed Balmer decrement between Hα and Hβ to correct all lines for foreground dust extinction, assuming an SMC-appropriate reddening law with $R_V = 2.74$ (Fitzpatrick & Massa 1990; Bouret et al. 2003). The reddening is low over most of the field ($E(B - V) \approx 0.1$) but reaches $E(B - V) \approx 1$ along the southern edge (labeled "foreground filament" in Figure 1b).

3. RESULTS FROM MUSE SPECTRA

An east-facing bow shock structure is detected around the star Walborn 3, as mapped in Figure 1, with emission line brightness profiles shown in Figure 2. The correspondence between different emission lines and the ionization state of the gas is illustrated in Figure 3, which explains the definitions of low, medium, and high ionization that we employ in this paper.

3.1. *Emission line maps*

Figure 1a shows that the inner edge of the bow shock is traced by a sharp ridge of the highest ionization He II $\lambda 4686$ emission (red), while [Ar IV] $\lambda 4740$ emission (green) is more extended and has a diffuse outer boundary. Nebular emission from the same field in medium and low ionization lines is shown in Figure 1b, from which one sees that there is no clear evidence for the bow shock in these lines. Instead, the low ionization lines ([O I], red, and [S II], green) trace the ionization fronts at the surface of dense filaments and globules, while the medium ionization line ([S III], blue) traces diffuse ionized gas in the interior of the nebula that is largely unrelated to the bow shock.

Figure 1c shows the position of the MUSE field (orange box) on a wider scale *HST* image of the N66 H II region (Nota et al. 2006). The head of the bow shock is oriented towards the bright N–S oriented filament that is located outside of the MUSE field to the West, and which represents a large scale ionization front at the edge of the H II region. The supernova remnant SNR J59.4−7210 is centered roughly 1 arcmin to the East of the H II region, but based on the X ray emission (Maggi et al. 2019) it does not overlap the MUSE field.

Figure 1d shows a zoomed view of the *HST* Hα image around W 3, compared with contours of the bow shock emission. The Hα brightness does appear to be slightly higher within the bow shock contours than just outside it, but the effect is subtle compared with the general fluctuations in Hα brightness in the nebula.

3.2. *Brightness profiles along the bow shock axis*

Figure 2a shows surface brightness profiles in multiple emission lines along an East–West cut along the bow shock axis. The He II emission peak lies at an offset 4 arcsec west from the star W 3, with a width (FWHM) of about 2 arcsec (note that 1 arcsec ≈ 0.3 pc at the distance of the SMC). If the He II line is due to recombination of He^{+2}, then a hard radiation field with $h\nu > 54.4$ eV is required in order to photoionize He^{+} (see Figure 3). The He II brightness becomes negative close to the star position due to contamination by the photospheric absorption line. The [Ar IV] emission peak lies slightly farther from the star (4.5 arcsec) and shows a gradual linear decline with FWHM ≈ 20 arcsec. In both lines, diffuse nebular emission is undetectably small in the regions adjoining the bow shock. The medium ionization lines, on the other hand, are dominated by the large-scale nebular emission and vary by a factor of only 1.5 to 2 along the entire slit. Nonetheless, there is an apparent rise in the brightness of these lines at the position of the bow shock (see gray box in Figure 2) that tracks the rise and fall of the [Ar IV] line. This increase amounts to about 50% of the diffuse nebular emission in the case of [O III] and the H and He recombination lines but only about 30% in the case of [Ar III], which is arises from lower ionization conditions than [O III], as shown in Figure 3.

Figure 2b shows even lower ionization emission, as traced by [S III] and [S II] lines, together with electron temperature and density profiles derived from the emission line ratios [S III] $\lambda 6312/\lambda 9069$ and [S II] $\lambda 6716/\lambda 6731$. The rise at the bow shock position is very weak in [S III] (about 15% of the diffuse nebula brightness) and it is completely absent in [S II]. The peaks in the [S II] profile at offsets of 7 arcsec and 12 arcsec correspond to ionization fronts of background globules, as seen in Figure 1b. The 12 arcsec peak is also visible in [S III] and the other medium ionization lines of panel a, but with lower contrast.

A broad maximum in [S III] lies at an offset of -3 arcsec and is labeled "medium-ionization peak" in the figure. It corresponds to whispy Hα emission seen in the HST image of Figure 1d immediately to the left of W 3. The same peak is also visible in the other medium ionization lines of Figure 2a, but the contrast decreases markedly as one passes from [S III], through [Ar III], to [O III], which is a sequence of increasing ionization (see Figure 3). This is the opposite behavior to what is seen at the position of the bow shock, where the order is reversed.

3.3. *[Ar IV] diagnostics*

4. LONGSLIT OBSERVATIONS

Apart from the inner rim of the bow shock, there is no diffuse He II emission in the core of NGC 346, or in the western side of the N66 region. The eastern side of N66, on

the other hand, shows extensive He II $\lambda 4686$ emission, as can be seen at offsets from -200 to -50 arcsec in Figure 5b. The
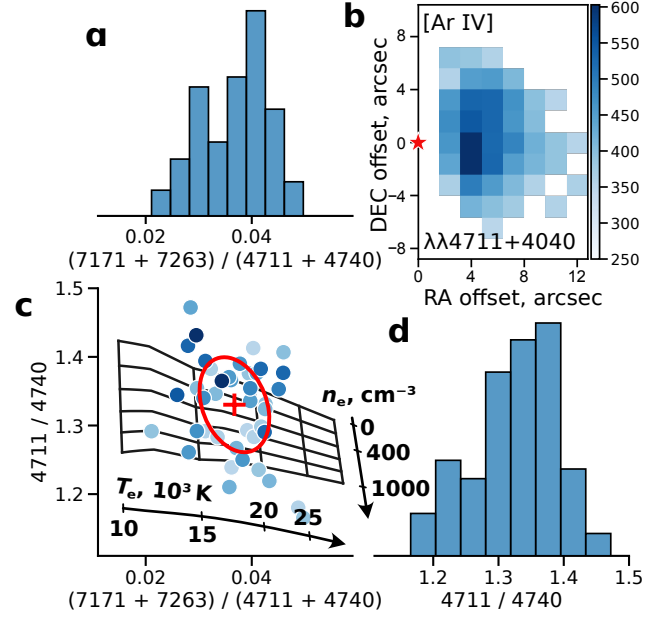

Figure 4. Temperature and density diagnostics of the bow shock from [Ar IV] line ratios.

eastern side of N66 also shows a ten times higher [Fe III] / Hβ ratio and disturbed kinematics in low-ionization lines such as [S II]. All these are probably due to a foreground supernova remnant SNR B0057−72.2 (Ye et al. 1991) that overlaps with this part of the nebula (Chu & Kennicutt 1988; Nazé et al. 2002; Danforth et al. 2003; Maggi et al. 2019; Matsuura et al. 2022).

5. MID-INFRARED EMISSION

6. DISCUSSION

Is there any possibility it might be a runaway?

What is the reason that we detect this bow shock at optical wavelengths, which is not typical? Probably due to the presence of the high ionization stages, which allow the weak bow shock emission to be separated from the background hii region. This is similar to the argument of (Danforth et al. 2003) as to why it is better to use UV observations to find SNR in bright hii regions.

7. CONCLUSIONS
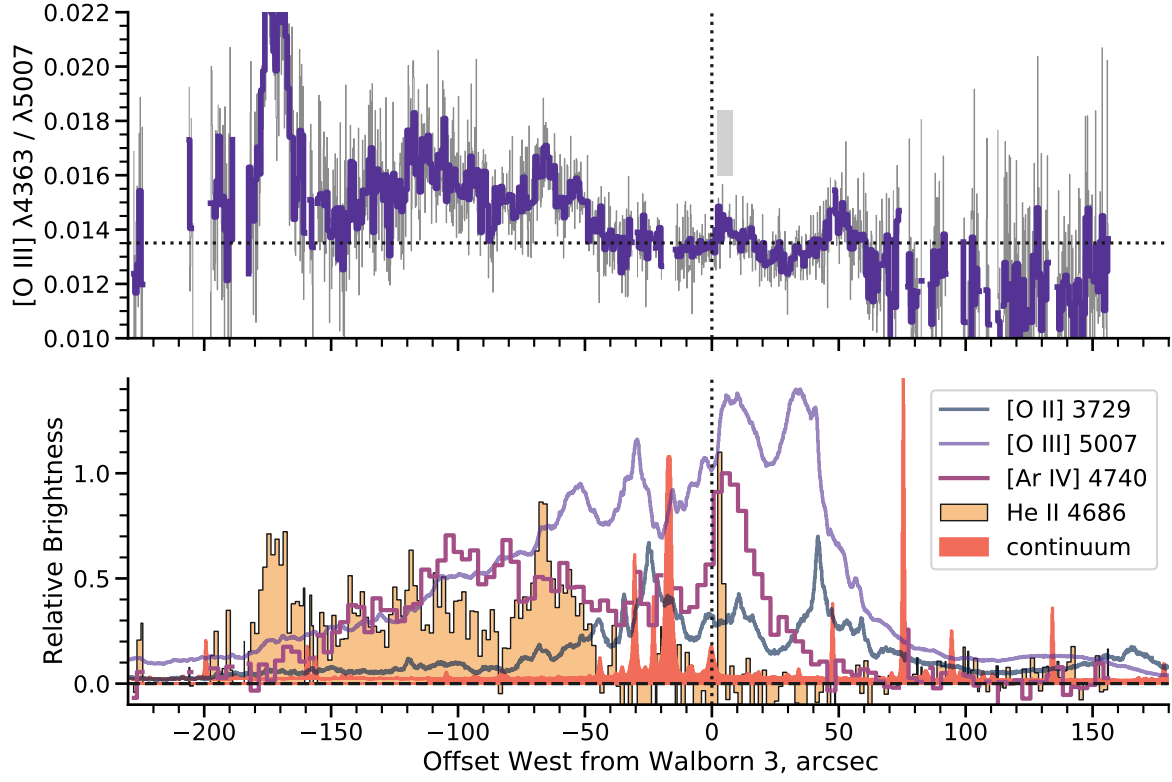
Thank you.

Facilities: VLT:Yepun (MUSE)

Figure 5. Emission line surface brightness profiles and line ratios along a large-scale East–West cut across the entire region, based on FORS1 longslit spectra. The slit is close to the symmetry axis of the bow shock. (a) Temperature-sensitive line ratio [O III] 4363/5007. The gray box shows the same inner rim region of the bow shock that is highlighted by a gray box in Fig. 2. (b) Selected emission lines from a wide range of ionization stages.
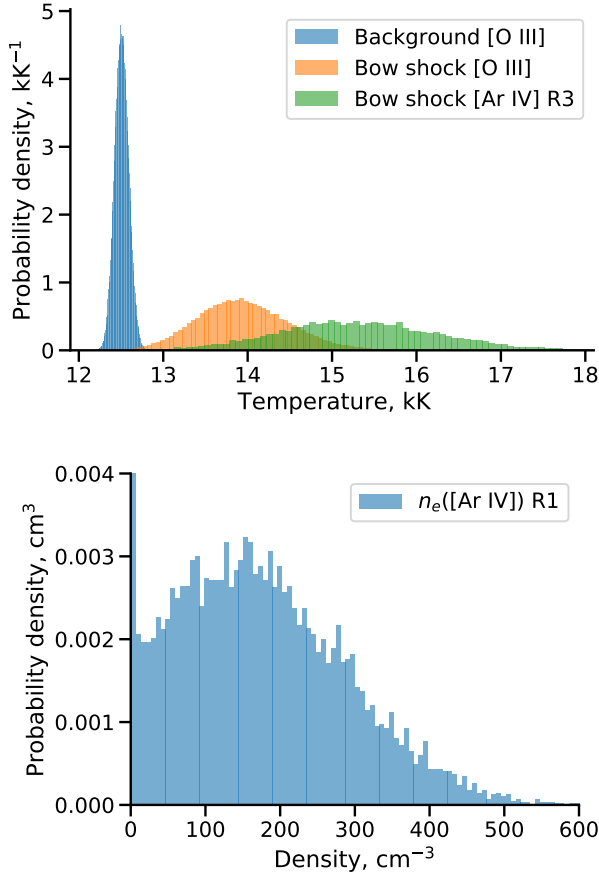
Figure 6. Derived temperature of nebula and bow shock from FORS longslit observations.

REFERENCES

Bacon, R., Accardo, M., Adjali, L., et al. 2010, in Society of Photo-Optical Instrumentation Engineers (SPIE) Conference Series, Vol. 7735, Proc. SPIE, 773508, doi: 10.1117/12.856027

Bacon, R., Vernet, J., Borisova, E., et al. 2014, The Messenger, 157, 13

Bally, J., & Reipurth, B. 2001, ApJ, 546, 299

Björklund, R., Sundqvist, J. O., Puls, J., & Najarro, F. 2021, A&A, 648, A36

Blaauw, A. 1961, BAN, 15, 265

Bouret, J. C., Lanz, T., Hillier, D. J., et al. 2003, ApJ, 594, 279, doi: 10.1086/376774

Chu, Y.-H., & Kennicutt, Robert C., J. 1988, AJ, 95, 1111

Cordes, J. M., Romani, R. W., & Lundgren, S. C. 1993, Nature, 362, 133

Cox, N. L. J., Kerschbaum, F., van Marle, A.-J., et al. 2012, A&A, 537, A35

Danforth, C. W., Sankrit, R., Blair, W. P., Howk, J. C., & Chu, Y.-H. 2003, ApJ, 586, 1179

Draine, B. T., & Li, A. 2007, ApJ, 657, 810

Fitzpatrick, E. L., & Massa, D. 1990, ApJS, 72, 163, doi: 10.1086/191413

Graczyk, D., Pietrzyński, G., Thompson, I. B., et al. 2020, ApJ, 904, 13

Gull, T. R., & Sofia, S. 1979, ApJ, 230, 782

Gvaramadze, V. V., Langer, N., & Mackey, J. 2012, MNRAS, 427, L50

Gvaramadze, V. V., Pflamm-Altenburg, J., & Kroupa, P. 2011, A&A, 525, A17

Henize, K. G. 1956, ApJS, 2, 315

Henney, W. J., & Arthur, S. J. 2019a, MNRAS, 486, 3423

—. 2019b, MNRAS, 486, 4423

—. 2019c, MNRAS, 489, 2142

Henney, W. J., García-Díaz, M. T., O'Dell, C. R., & Rubin, R. H. 2013, MNRAS, 428, 691

Heydari-Malayeri, M., & Selier, R. 2010, A&A, 517, A39

Hillier, D. J. 2020, Galaxies, 8, 60

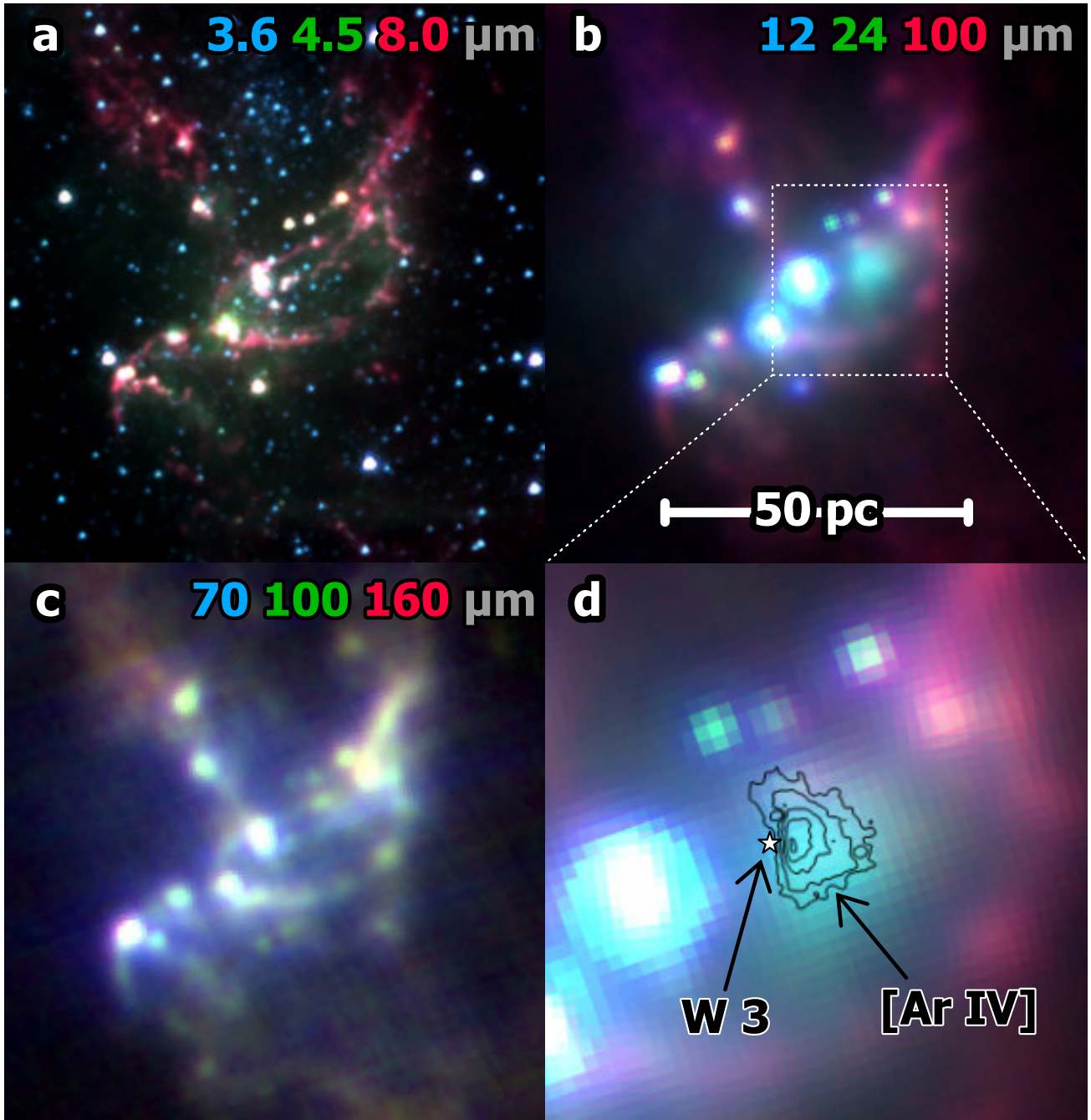Hoogerwerf, R., de Bruijne, J. H. J., & de Zeeuw, P. T. 2001, A&A, 365, 49

Figure 7. Panoramic view of the NGC 346/N66 region at infrared wavelengths: (a) Short wavelength mid-infrared (3.6 to 8 μm); (b) Longer wavelength mid-infrared (12 to 100 μm); (c) Far-infrared (70 to 150 μm); (d) Zoomed view of panel b. Images are from satellite observatories as follows: *Spitzer* IRAC 3.6, 4.5, 8 μm); *WISE* 12 μm; *Spitzer* MIPS 24, 70 μm; *Herschel* PACS 100, 150 μm.

Kobulnicky, H. A., Chick, W. T., & Povich, M. S. 2018, ApJ, 856, 74 (K18)

—. 2019, AJ, 158, 73

Kobulnicky, H. A., Chick, W. T., Schurhammer, D. P., et al. 2016, ApJS, 227, 18

Krtička, J., & Kubát, J. 2018, A&A, 612, A20

Mackey, J., Gvaramadze, V. V., Mohamed, S., & Langer, N. 2015, A&A, 573, A10

Mackey, J., Haworth, T. J., Gvaramadze, V. V., et al. 2016, A&A, 586, A114

Maggi, P., Filipović, M. D., Vukotić, B., et al. 2019, A&A, 631, A127, doi: 10.1051/0004-6361/201936583

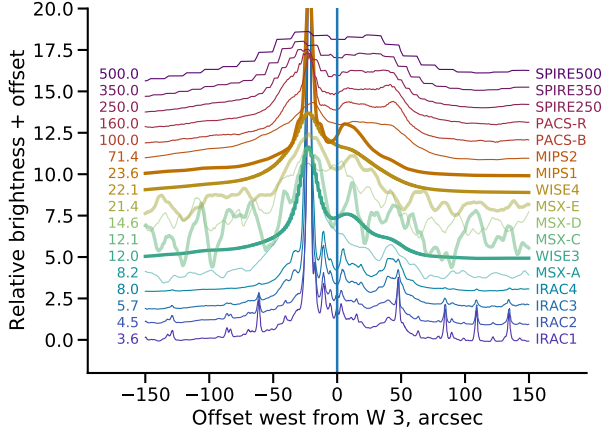Massey, P., Parker, J. W., & Garmany, C. D. 1989, AJ, 98, 1305

Figure 8. East–west brightness profile cuts in various infrared bands.
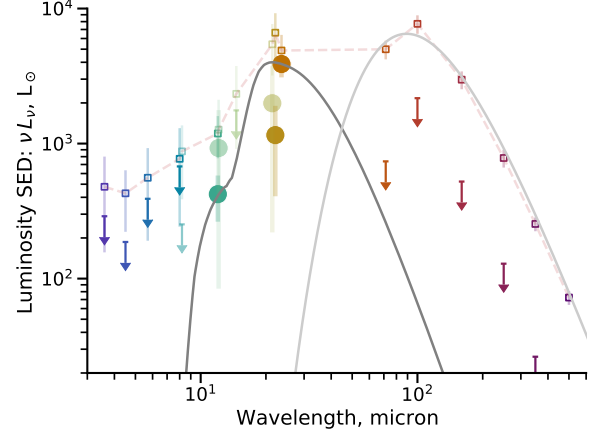

Figure 9. Spectral energy distribution of bow shock (large symbols and downward arrows) and background nebula small symbols joined by dashed line.

Matsuura, M., Ayley, V., Chawner, H., et al. 2022, MNRAS, 513, 1154, doi: 10.1093/mnras/stac583

Meyer, D. M.-A., van Marle, A.-J., Kuiper, R., & Kley, W. 2016, MNRAS, 459, 1146

Narloch, W., Pietrzyński, G., Gieren, W., et al. 2021, A&A, 647, A135

Nazé, Y., Hartwell, J. M., Stevens, I. R., et al. 2002, ApJ, 580, 225

Nota, A., Sirianni, M., Sabbi, E., et al. 2006, ApJL, 640, L29, doi: 10.1086/503301

Povich, M. S., Benjamin, R. A., Whitney, B. A., et al. 2008, ApJ, 689, 242

Renzo, M., Zapartas, E., de Mink, S. E., et al. 2019, A&A, 624, A66

Rivero González, J. G., Puls, J., Massey, P., & Najarro, F. 2012, A&A, 543, A95

Sahai, R., & Chronopoulos, C. K. 2010, ApJL, 711, L53

Sheets, H. A., Bolatto, A. D., van Loon, J. T., et al. 2013, ApJ, 771, 111

Tenorio-Tagle, G. 1979, A&A, 71, 59

van Buren, D., & McCray, R. 1988, ApJL, 329, L93

van Buren, D., Noriega-Crespo, A., & Dgani, R. 1995, AJ, 110, 2914

Vink, J. S., de Koter, A., & Lamers, H. J. G. L. M. 2001, A&A, 369, 574

Vink, J. S., & Sander, A. A. C. 2021, MNRAS, 504, 2051

Walborn, N. R., & Blades, J. C. 1986, ApJL, 304, L17

Weilbacher, P. M., Palsa, R., Streicher, O., et al. 2020, A&A, 641, A28, doi: 10.1051/0004-6361/202037855

Wilkin, F. P. 1996, ApJL, 459, L31

Ye, T., Turtle, A. J., & Kennicutt, R. C., J. 1991, MNRAS, 249, 722